Journal of Geophysical Research: Oceans

RESEARCH ARTICLE
10.1029/2017JC013591

# Internal Tide Dissipation at Topography: Triadic Resonant Instability Equatorward and Evanescent Waves Poleward of the Critical Latitude

**O. Richet**[1], **J.-M. Chomaz**[1], **and C. Muller**[2]

[1]LadHyX, École polytechnique, Palaiseau, France, [2]Laboratoire de Météorologie Dynamique, École Normale Supérieure, Paris, France

**Key Points:**
- Triadic instabilities involving inertial waves are responsible for the dissipation of internal tides equatorward of the critical latitude
- The 2*f*-pump mechanism is found to be an efficient mechanism to dissipate internal tide energy poleward of the critical latitude
- The sensitivities of triadic instabilities and of evanescent wave generation to latitude explains the strong enhancement of internal tide dissipation near the critical latitude

**Correspondence to:**
O. Richet,
oceane.richet@ladhyx.polytechnique.fr

**Citation:**
Richet, O., Chomaz, J.-M., & Muller, C. (2018). Internal tide dissipation at topography: Triadic resonant instability equatorward and evanescent waves poleward of the critical latitude. *Journal of Geophysical Research: Oceans*, *123*, 6136–6155. https://doi.org/10.1029/2017JC013591

Received 27 OCT 2017
Accepted 10 MAY 2018
Accepted article online 25 MAY 2018
Published online 3 SEP 2018



**Abstract** Several studies have shown the existence of a critical latitude where the dissipation of internal tides is strongly enhanced. Internal tides are internal waves generated by barotropic tidal currents impinging rough topography at the seafloor. Their dissipation and concomitant diapycnal mixing are believed to be important for water masses and the large-scale ocean circulation. The purpose of this study is to clarify the physical processes at the origin of this strong latitudinal dependence of tidal energy dissipation. We find that different mechanisms are involved equatorward and poleward of the critical latitude. Triadic resonant instabilities are responsible for the dissipation of internal tides equatorward of the critical latitude. In particular, a dominant triad involving the primary internal tide and near-inertial waves is key. At the critical latitude, the peak of energy dissipation is explained by both increased instability growth rates, and smaller scales of secondary waves thus more prone to break and dissipate their energy. Surprisingly, poleward of the critical latitude, the generation of evanescent waves appears to be crucial. Triadic instabilities have been widely studied, but the transfer of energy to evanescent waves has received comparatively little attention. Our work suggests that the nonlinear transfer of energy from the internal tide to evanescent waves (corresponding to the 2*f*-pump mechanism described by Young et al., 2008, https://doi.org/10.1017/S0022112008001742) is an efficient mechanism to dissipate internal tide energy near and poleward of the critical latitude. The theoretical results are confirmed in idealized high-resolution numerical simulations of a barotropic M2 tide impinging sinusoidal topography in a linearly stratified fluid.

## 1. Introduction

Internal waves are ubiquitous in the ocean and they play a key role in the circulation and the stratification of the ocean (Garrett & Munk, 1979). They permit energy transfer from mesoscale flows to small spatial scales, where they are dissipated and induce diapycnal mixing (Munk & Wunsch, 1998; Wunsch & Ferrari, 2004). Interest in internal waves dynamics has been enhanced in the last decades with parametrization of internal waves-driven mixing in the global climate models, and its impact on the large-scale ocean properties (Ferrari et al., 2016; Melet et al., 2016; Talley, 2013). Far from the Antarctic Circumpolar Current (ACC), diapycnal mixing is primarily induced by abyssal internal tides (De Lavergne et al., 2016a, 2016b; Nikurashin & Ferrari, 2013), which are internal waves generated by barotropic tide current impinging rough topography (Garrett & Kunze, 2007).

For the purpose of understanding the dynamics of internal tides, several numerical studies considered the dissipation of semidiurnal internal tide (generated by topography interacting with the semidiurnal barotropic M2 tide) (Gerkema et al., 2006; Hibiya et al., 2002; MacKinnon & Winters, 2005; Nikurashin & Legg, 2011; Richet et al., 2017). They showed a strong latitudinal distribution and the existence of a critical latitude where dissipation is strongly enhanced. This critical latitude exhibits enhanced dissipation of both low-mode (MacKinnon & Winters, 2005) and high-mode internal tide (Nikurashin & Legg, 2011; Richet et al., 2017). The critical latitude corresponds to the latitude where the Coriolis frequency $f$ matches half the tidal semidiurnal frequency $\omega_0$: $f \approx \omega_0/2$ and is approximately equal to 29°. Observations confirm the enhancement of dissipation near the critical latitude, albeit with weaker amplitude than expected from numerical studies (Alford et al., 2007; MacKinnon et al., 2013). One possible explanation for this amplitude discrepancy is the Doppler effect due to background oceanic currents, which spreads the dissipation over a wider range of critical latitudes (Richet et al., 2017). Apart from this consideration, MacKinnon and Winters (2005), Hazewinkel and

Winters (2011), and Nikurashin and Legg (2011) showed that one mechanism to explain the latitudinal dependence of internal tide dissipation (without a background current) is the Parametric Subharmonic Instability (PSI). In this paper, we propose to complete Nikurashin and Legg's (2011) numerical study on high-mode internal tide and investigate in detail (theoretically and numerically) two physical processes leading to the distribution of M2 internal tide dissipation with latitude: the triadic resonant instability equatorward and the 2*f*-pump mechanism (Young et al., 2008) poleward of the critical latitude.

PSI is a weakly nonlinear resonant phenomenon (e.g., McComas & Bretherton, 1977; Young et al., 2008) in which the energy is transferred from the primary internal tide to two secondary waves at approximately half the tidal frequency. These secondary waves have smaller wavelength than the primary wave, they reach large amplitude through the energy transfer, break and dissipate their energy under shear instability, yielding the mixing ultimately relevant to the large-scale ocean circulation (Staquet & Sommeria, 2002). Thereby PSI is an efficient mechanism promoting shear instability and breaking, transferring energy to smaller vertical scales. More generally, the instability of a primary wave producing two secondary waves which match resonant conditions is named a triadic resonant instability (TRI).

Equatorward of the critical latitude, we investigate whether TRI is the most efficient mechanism that dissipates internal tide energy, and which triads are involved in these energy transfers (see section 4 for more details on the TRI). Two candidates in the literature are triads with secondary waves at frequencies $\omega_1=\omega_2=\omega_0/2$ (MacKinnon & Winters, 2005), or $\omega_1=f$ and $\omega_2=\omega_0-f$ (Nikurashin & Legg, 2011). Note that in both cases, these secondary waves satisfy the resonance conditions $\omega_0=\omega_1+\omega_2$. Poleward of the critical latitude, one of the waves would have a frequency below *f* for both of those triads, which is impossible since it would be then not within the range of internal wave frequencies (internal waves have frequencies between *f* and the stratification frequency *N*), so there is no resonant triad. Another dissipation mechanism has been proposed and will be investigated here, the "2*f*-pump" (Korobov & Lamb, 2008; Young et al., 2008). The 2*f*-pump is an extension of PSI in a rotating frame, with the generation of near-inertial secondary waves which are *evanescent*. This physical process can extract energy from the primary internal tide at $\omega_0$ to evanescent secondary waves at $\omega_0/2$. We will investigate whether this process plays a role in our simulations and whether it can lead to strong dissipation poleward of the critical latitude.

The purpose of this study is to explain the physical mechanisms behind the latitudinal distribution of internal tide energy dissipation by confronting theoretical results with numerical simulations. Section 2 of the paper describes the equations governing the motion of internal waves and the setup of the numerical simulations. Section 3 is an overview of the numerical results, where we split the latitudinal dynamics of internal tides into two parts: part I, equatorward of the critical latitude, where internal tides are propagating waves and transfer their energy through triadic resonant instabilities, and part II, poleward of the critical latitude, where there is the possibility of energy transfer to secondary evanescent waves via the 2*f*-pump. Sections 4 and 5 investigate in detail the mechanisms of dissipation in these two parts. Results are summarized and conclusions are offered in section 6.

## 2. Methods

### 2.1. Theoretical Background: Equations of Motion

Internal waves are waves found in stratified fluids. In this section, we derive their dispersion relation from a simplified set of equations, namely the Boussinesq equations on the *f*-plane assuming constant stratification. Under the Boussinesq approximation, the total density is $\rho(x,z,t)=\rho_0+\rho_s(z)+\sigma(x,z,t)$, where $\rho_0$ is assumed constant, and $\rho_s$ is linked to the background vertical stratification corresponding to the Brunt-Väisälä frequency *N* satisfying $N^2=-(g/\rho_0)(d\rho_s/dz)$ assumed constant. We introduce the buoyancy related to the density perturbation $b=-(g/\rho_0)\sigma$. Internal waves are governed by the nonlinear Boussinesq equations of motion on the *f*-plane:

$$\frac{D}{Dt}\mathbf{u}+f\hat{\mathbf{z}}\times\mathbf{u}=-\frac{1}{\rho_0}\nabla p+b\hat{\mathbf{z}}+\nu\nabla^2\mathbf{u}, \tag{1}$$

$$\frac{D}{Dt}b+N^2w=\kappa\nabla^2 b, \tag{2}$$

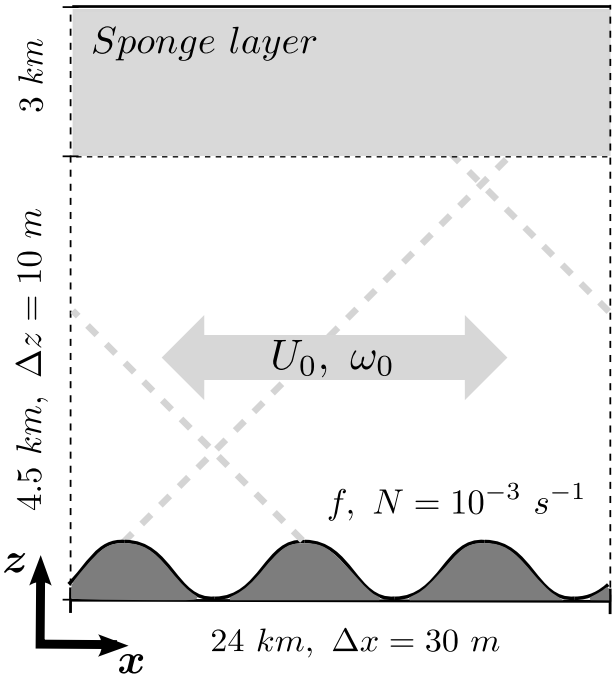


**Figure 1.** Schematic of the numerical setup. The barotropic tidal current, with amplitude $U_0$ and frequency $\omega_0$ interacts with a one-dimension sinusoidal topography in a linearly stratified ($N$ constant) and rotating ($f$ constant) fluid and generates internal tides (oblique dashed lines). The gray shaded area at the top of the domain represents the sponge layer.

$$\nabla\cdot\mathbf{u}=0. \tag{3}$$

We reduce the set of equations to the 2-D case ($x$, $z$), considering $\partial/\partial y \equiv 0$. Nevertheless, we allow for a velocity $v$ in the $y$ direction. The model is a 2-D model with three components. This assumption is relevant if we consider that roughness of ridges is nearly two-dimensional. $D/Dt$ denotes the Lagrangian derivative, and we solve the equations for flow velocity $\mathbf{u}=(u,v,w)$ and buoyancy $b$. $\nu$ denotes the viscosity and $\kappa$ denotes the diffusivity. For simplicity, we assume that the diffusion term is negligible.

If we linearize this set of equations about a state of rest neglecting viscosity, and look for wave solutions of the form $\propto e^{i(kx+mz-\omega t)}$, we obtain the dispersion relation of internal waves:

$$\omega^2=N^2\sin^2\theta+f^2\cos^2\theta=\frac{N^2k^2+f^2m^2}{K^2}, \tag{4}$$

with $\omega$ the frequency of the internal wave, $\theta$ is the angle of energy propagation with the horizontal such that $\mathbf{k}=(k,0,m)=K(\sin\theta,0,\cos\theta)$ where $K$ is the magnitude of the wave vector $\mathbf{k}$. We see that propagating waves (i.e., with real $\omega, k$ and $m$), necessarily have their frequency $\omega\in[f,N]$ ($f<N$ typically in the ocean).

### 2.2. Numerical Simulations Configuration

For the numerical simulations, we use the Massachusetts Institute of Technology Global Circulation Model (MITgcm; Marshall et al., 1997), a high-resolution numerical model in nonhydrostatic configuration. The nonhydrostatic configuration allows the explicit representation of processes such as hydraulic jumps or Kelvin-Helmholtz instabilities. The model is developed with the finite-volume method to provide the treatment of irregular geometries like the topography using the MITgcm partial cells' architecture. The bottom boundary is treated with a no-slip condition.

The main characteristics of the domain are summarized in Figure 1. The domain is two-dimensional and periodic in the $x$ direction. The horizontal size of the domain is 24 km with a uniform resolution of 30 m. The vertical extent of the domain is equal to 7.5 km, organized in two layers: the 4.5 km bottom layer and the 3 km sponge layer at the top. Indeed, the goal of this paper is to highlight the mechanisms by which internal tides dissipate locally near their generation site. In fact, a major unknown is the fraction of internal waves that dissipate locally near the seafloor and the fraction of internal tides that escape and dissipate remotely, which can influence the upwelling of Antarctic Bottom Water, contributing to circulation values varying from 1 to 28 Sv (1 Sv $=10^6$ m$^3$ s$^{-1}$) (De Lavergne et al., 2016a). A better understanding of the fraction of internal tides which dissipate locally near their generation site is needed to evaluate the fraction of internal tides that escape and are available to dissipate remotely. This is the question addressed here, namely what is the fraction of internal tide energy dissipated locally. For practical reason, we neglect the reflection of the waves at the ocean surface and their interactions with the thermocline. In other words, we consider a semi infinite ocean, and for this purpose we impose a sponge layer at the top of the ocean interior to absorb upward-propagating waves which are not dissipated locally. In the sponge layer, momentum and buoyancy are damped with a linear drag with a time scale of 1 h. The bottom layer corresponding to the ocean interior has a uniform resolution of 10 m. The resolution of the sponge layer is progressively stretched from 10 m at the base of the layer to 70 m at the top. The model time step is 30 s. These high-resolution idealized simulations are designed to allow the resolution of a wide range of spatial and temporal scales of the turbulence.

In the simulations, the fluid is linearly stratified in the vertical with constant buoyancy frequency $N=10^{-3}$ s$^{-1}$, representative of the deep ocean stratification. Following Richet et al. (2017), the viscosity (horizontal and vertical) is equal to $\nu=2\times10^{-3}$ m$^2$ s$^{-1}$ and the diffusivity (horizontal and vertical) is set to $\kappa=10^{-4}$ m$^2$ s$^{-1}$.

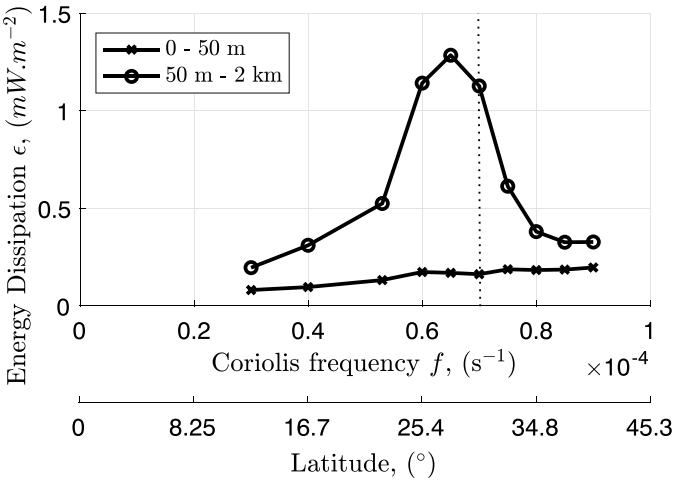


**Figure 2.** Energy dissipation rate integrated in the bottom 50 m (cross) and between 50 m and 2 km (circle). The vertical black dotted line indicates the critical latitude. Each point corresponds to a simulation at a given latitude ($f$ constant) and the viscous energy dissipation is averaged over $x$ direction and over the last 10 days of simulation, and integrated over 0–50 m above topography for the bottom boundary layer, and over 50 m to 2 km for the ocean interior.

The Coriolis frequency $f$ is set to be constant for each given simulation. To investigate the latitudinal variation of internal tide dissipation, we vary $f$ between simulations.

Internal tides are generated by the barotropic flow interacting with an idealized sinusoidal topography. The simulations are initiated from a state of rest and run for 30 days (a statistically steady state is reached in 5–10 days). The tidal barotropic flow is imposed by adding a body force to the momentum equations, yielding a barotropic semidiurnal lunar $M_2$ tide, $U(t)=U_0\sin(\omega_0 t)$ with an amplitude $U_0=2.5$ cm s$^{-1}$ and the tidal frequency $\omega_0=1.4\times10^{-4}$ s$^{-1}$.

The choice of a simple idealized sinusoidal topography is motivated by the fact that the dissipation profiles and magnitudes are found to be similar to those obtained with a realistic topography spectrum, as long as the vertical and horizontal Froude numbers are the same (Richet et al., 2017). We therefore use the realistic horizontal and vertical Froude numbers $\mathrm{Fr}_h=U_0/(N2\pi/k_0)\approx4\times10^{-3}$ and $\mathrm{Fr}_v=U_0/(Nh)\approx10^{-1}$, where $k_0=8\times10^{-4}$ m$^{-1}$ is the horizontal wave number and $h=110$ m is the rms height of the sinusoidal topography. With this choice, the sensitivity of dissipation to latitude and the physical processes involved in our simulations is relevant, at least qualitatively, to more realistic conditions representative of the deep ocean in the region of the Brazil Basin (Nikurashin & Legg, 2011; Richet et al., 2017).

## 3. Overview of Numerical Results: Latitudinal Distribution of Tidal Dissipation and Physical Processes Involved

The purpose of this study is to explain the physical mechanisms behind the latitudinal distribution of internal tide energy dissipation. From numerical results, we give a first glimpse of possible mechanisms and their repartition with latitude before studying them in detail and validating their existence and their efficiency for the dissipation of internal tide energy in following sections.

Nikurashin and Legg (2011) and Richet et al. (2017) show a strong dependence of internal tide energy dissipation with latitude. Figure 2 summarizes these results. From the equator toward the critical latitude, the energy dissipation increases slowly at the beginning and strongly after ~22° of latitude ($f=0.53\times10^{-4}$ s$^{-1}$). Poleward of the critical latitude, energy dissipation decreases and becomes constant after ~35° of latitude ($f=0.8\times10^{-4}$ s$^{-1}$). We divide the curve into two parts: part I equatorward of the critical latitude where secondary waves, in particular at $\omega_0/2$ or $\omega_0-f$, are propagating, i.e., their frequency is in the internal wave range $[f, N]$, see equation (4); and part II poleward of the critical latitude where those secondary waves are evanescent.

Figure 3 shows kinetic energy density spectra from simulations at $f=0.53\times10^{-4}$ and $f=0.75\times10^{-4}$ s$^{-1}$ averaged over 5–30 days. Equatorward of the critical latitude (Figure 3a), dominant frequencies in the domain are $\omega_0$, the primary internal tide, but also waves at frequency $f$, i.e., inertial waves, and at frequencies $(\omega_0-f)$ (and with smaller amplitude $\omega_0+f$). These results suggest that the physical mechanism responsible for the energy transfer from internal tides to smaller-scale secondary waves is the formation of resonant triads between the primary internal tide, inertial waves and waves at frequencies $(\omega_0-f)$, and to a lesser extent $(\omega_0+f)$. Poleward of the critical latitude (Figure 3b), the dominant frequencies in the kinetic energy spectrum are the primary internal tide at $\omega_0$ and the evanescent wave at $\omega_0/2$ ($\omega_0/2<f$). This result suggests the transfer of energy to smaller-scale evanescent near-inertial waves as the dominant physical process leading to the dissipation of the primary internal tide.

The latitudinal evolution of the amplitude of the main wave frequency peaks, measured on integrated spectra like the one presented on Figure 3, are summarized in Figure 4. Equatorward of the critical latitude, the enhancement of energy dissipation seems to be linked to a strong generation of inertial waves accompanied by waves at $\omega_0-f$. The waves at $\omega_0+f$ do not play a leading-order role. It should be noted here and it will be

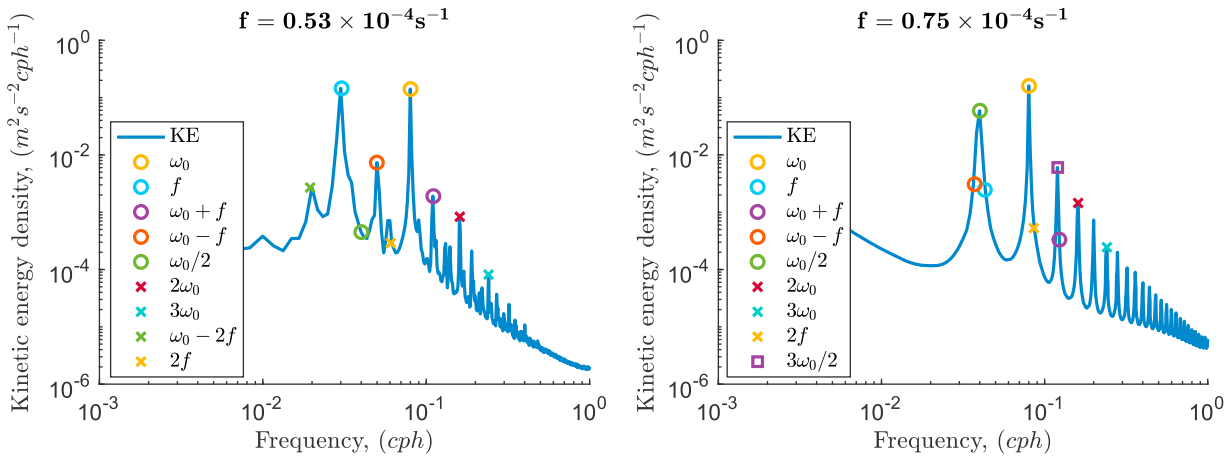


**Figure 3.** Kinetic energy density spectra from simulations at (a) $f$=0.53×10$^{-4}$ s$^{-1}$ and (b) $f$=0.75×10$^{-4}$ s$^{-1}$. Spectra are calculated over the period of 5–30 days and averaged zonally and over the region 500 m above topography.

proved later that the triad involving $\omega_0+f$ is not an unstable triad. Poleward of the critical latitude, the dissipation seems to be dominated by energy transfers to secondary waves at $\omega_0/2$.

These results suggest two different mechanisms for internal tides dissipation in the two regions previously defined: equatorward of the critical latitude (part I) and poleward of the critical latitude (part II). Equatorward of the critical latitude, dissipation of internal tides seems to involve triadic resonant instabilities. Poleward of the critical latitude, dissipation seems to be linked to the energy transfer to evanescent waves. In the next sections, we investigate in detail those physical mechanisms and provide further evidence for their key role in the dissipation of tidal energy.

## 4. Part I—Equatorward of the Critical Latitude: Triadic Resonant Instabilities (TRI)

In order to explain the latitudinal dependence of the energy dissipation equatorward of the critical latitude, we investigate theoretically resonant triads. We will see that the energy transfers occur in three stages. During the first stage, corresponding to the beginning of the simulation, secondary waves with a wide range of frequencies are generated by triadic resonant instability from the primary internal tide. A second stage consists of an accumulation of inertial waves close to topography. Finally, in a third stage, the dominant triadic resonant instability appears between the primary internal tide and the inertial waves, strengthening the generation of waves at frequencies $(\omega_0 - f)$.

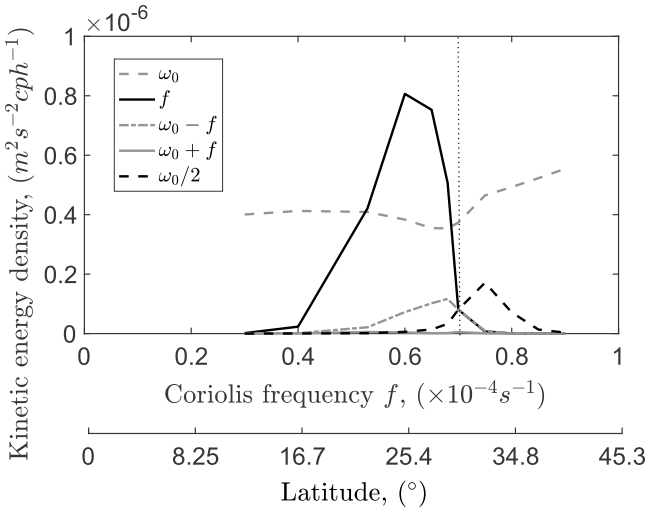


**Figure 4.** Latitudinal evolution of the kinetic energy density for the leading frequencies in the domain: the primary internal tide $\omega_0$ (gray dashed), inertial waves $f$ (black plain) and waves at frequencies $(\omega_0 - f)$ (gray point-dashed), $(\omega_0+f)$ (gray plain—here nearly indistinguishable from the axis), and $\omega_0/2$ (black dashed). The vertical black dotted line materializes the critical latitude. The amplitude of the different frequencies is measured on integrated spectra like the one presented in Figure 3.

### 4.1. Triadic Resonant Instability Theory

The instability of a primary wave producing two secondary waves which match the resonant conditions of triadic resonant instability (TRI) has been confirmed experimentally in a rotating tank (Maurer et al., 2016). However, the constraints associated with laboratory experiments, in particular size constraints, imply that the Reynolds number is low, in other words viscous effects are much stronger than in the ocean, and this can impact energy transfer in triads. Here we revisit and expand the generation of triads via the TRI observed and studied theoretical in a rotating frame in Maurer et al. (2016), in numerical simulations more representative of the oceanic conditions.

#### 4.1.1. Unstable Triads and Growth Rate

Following Maurer et al. (2016), we consider that only the primary wave with stream function amplitude $\Psi_0$ (see Appendix A for the stream

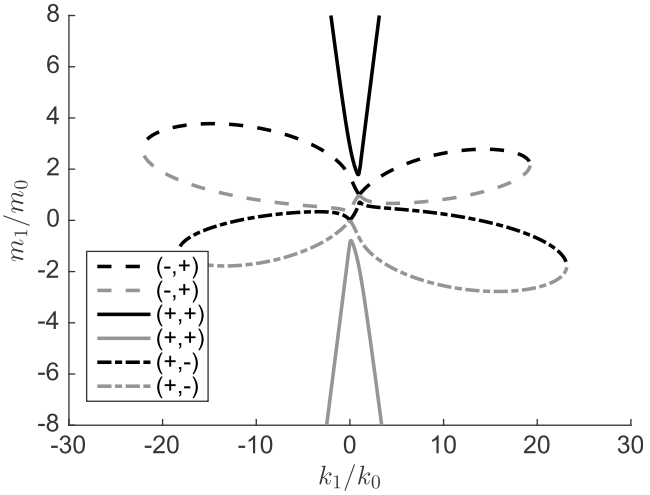


**Figure 5.** The curves represent the location of ($k_1$, $m_1$) satisfying equation (7) at $f=0.53\times10^{-4}$ s$^{-1}$ for the three possible combinations of signs and for the realistic parameter values used in our simulations. Plain lines represent unstable branches associated to (+,+) combination signs, while dashed lines correspond to neutrally stable cases.

function form of equations 1–3) frequency $s_0\omega_0$ (by convention, we consider $\omega_0 > 0$ and $s_0$ is its sign) wave vector $\mathbf{k_0}=(k_0, m_0)$ is present initially in the system. We impose $m_0 < 0$ to match the numerical simulation where the primary internal tide is generated at the topography and propagates upward (i.e., has positive vertical group velocity, which for internal waves is equivalent to negative vertical phase velocity). The secondary waves with amplitudes $\Psi_{1,2}$ are present as noise. The two secondary waves $(s_1, \omega_1, \mathbf{k_1})$ and $(s_2, \omega_2, \mathbf{k_2})$ form a resonant triad with the primary wave, satisfying the spatial resonant condition

$$\mathbf{k_0}=\mathbf{k_1}+\mathbf{k_2}, \tag{5}$$

and the temporal resonance condition

$$s_0\omega_0=s_1\omega_1+s_2\omega_2. \tag{6}$$

In all calculations, we consider that wave frequencies $\omega_{0,1,2}$ are positive, while $s_{0,1,2}$ are their signs. Using the dispersion relation for internal waves (equation (4)), the resonant conditions lead to

$$s_0\sqrt{\frac{k_0^2N^2+m_0^2f^2}{\kappa_0^2}}=s_1\sqrt{\frac{k_1^2N^2+m_1^2f^2}{\kappa_1^2}}+s_2\sqrt{\frac{(k_0-k_1)^2N^2+(m_0-m_1)^2f^2}{(k_0-k_1)^2+(m_0-m_1)^2}}. \tag{7}$$

Without loss of generality, we can set $s_0=+1$. For a given primary wave $(s_0, k_0, m_0)$, the solution of this equation for each sign combination $(s_0=+1, s_1, s_2)$ is the curve in the ($k_1$, $m_1$)-plane shown in Figure 5 using the stratification value $N=10^{-3}$ s$^{-1}$ representative of the deep ocean, and a value of $f$ equatorward of the critical latitude $f=0.53\times10^{-4}$ s$^{-1}$. We use the same sign convention on wave frequencies as Bourget et al. (2013) and Maurer et al. (2016), leading to similar results. But Figure 5 as well as the growth rates in Figure 6 show differences compared to these experimental studies. This is because of the oceanic parameter values used here, while their values were constrained by the laboratory experiments. In particular, Maurer et al. (2016) are constrained by the limited spatial scales allowed in experiments, and have a Reynolds number $Re$~200. In our simulations, the Reynolds number is more turbulent and thus closer to the oceanic regime with a $Re$~$10^4$.

As the sign of the primary wave is imposed, we have to consider four sign combinations for ($s_1$, $s_2$): (−,−), (+,+), (−,+), and (+,−). First of all, no solution exists for the combination (−,−). To know which branch, defined by the sign combination, is stable or unstable, we calculate the associated growth rate $\sigma$ given by (see full calculation and definition of coefficients $I_1$ and $I_2$ in Appendix A):

$$\sigma=-\frac{\nu}{4}\left(\kappa_1^2+\kappa_2^2+\frac{f^2m_1^2}{\omega_1^2}+\frac{f^2m_2^2}{\omega_2^2}\right)+\sqrt{\frac{\nu^2}{16}\left(\kappa_1^2-\kappa_2^2+\frac{f^2m_1^2}{\omega_1^2}-\frac{f^2m_2^2}{\omega_2^2}\right)^2+I_1I_2|\Psi_0|^2}. \tag{8}$$

A negative growth rate corresponds to a stable branch (dashed curves in Figure 5) and is not relevant for this study, which is the case for combinations (+,−) and (−,+). The study will focus only on the (+,+) combination which has a positive growth rate and hence corresponds to an unstable branch (plain curves in Figure 5). In the simulations, we expect to observe a transfer of energy to the most unstable secondary waves (i.e., with the largest growth rate).

Without loss of generality, we can limit our analysis to the upper branch: the upper and lower branches (+,+) correspond to exchanging the labels 1 and 2 between $(\omega_1, \mathbf{k}_1)$ and $(\omega_2, \mathbf{k}_2)$, and thus show the same triad ($\omega_0$ primary wave yields $\omega_1$ and $\omega_2$ secondary waves). It follows from equation (5) that they are obtained from one another by symmetry with respect to $\mathbf{k_0}/2$.

Figure 6 shows the growth rate $\sigma$ associated with the upper unstable branch as a function of the secondary waves frequencies ($\omega_1$ or $\omega_2$), calculated for each point of the upper branch of Figure 5. Despite a weak maximum growth rate $\sigma_{max}$, we see that the temporal growth rate is roughly constant over a wide range of

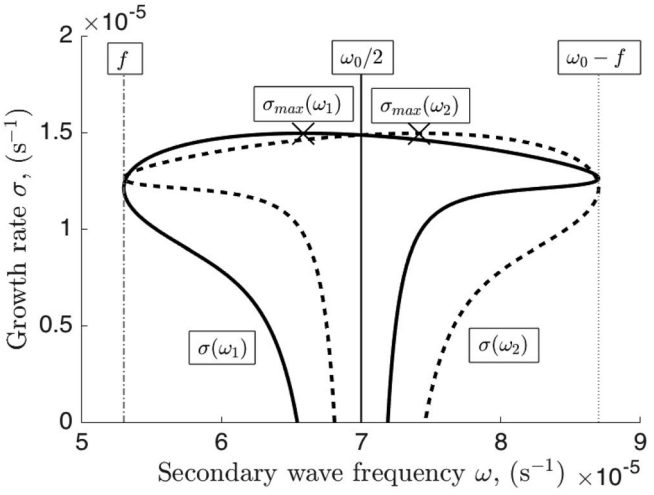


**Figure 6.** Growth rate $\sigma$ as a function of the frequency of secondary waves associated with the upper unstable branch (plain black line in Figure 5) for $f=0.53\times 10^{-4}$ s$^{-1}$. The plain curve represents the growth rate as a function of the frequency of the first secondary wave $\omega_1$, and the dashed curve represents the growth rate as a function of the frequency of the second secondary wave $\omega_2$.

frequencies (between $f$ and $\omega_0 - f$). In other words, no specific triad is selected. We therefore expect in the simulations that TRIs generate, from the primary internal tide, secondary waves with a wide range of frequencies.

It should be noted that as $f$ is increased toward $\omega_0/2$ the unstable branch gets more and more folded with a cusp moving to infinite vertical wave number when approaching $\omega_0/2$ (see Figure 7a). No triadic instability is possible after the critical latitude $f=\omega_0/2$. We will come back to internal tide dissipation poleward of the critical latitude in section 5.

Hence, the theory of TRI, applied with oceanic parameters, predicts the generation, from the primary tide, of secondary waves with a wide range of frequencies. In section 4.2, this theoretical result is compared to numerical simulations to validate TRI as the principal mechanism in internal tide dissipation equatorward of the critical latitude.

#### 4.1.2. Evolution of Dissipation From the Equator Toward the Critical Latitude

Internal tide energy dissipation increases significantly as the critical latitude is reached (see Figure 2). In this section, we investigate the effect of the latitude on TRI growth rate and secondary waves, in order to explore the reason behind the increase of dissipation at the critical latitude.

Figure 7 shows for different latitudes the loci of TRI and the associated growth rate of the unstable branches as a function of the frequency of secondary waves. From the equator ($f=0$ s$^{-1}$) toward the critical latitude, the unstable branch goes to infinite vertical wave numbers and tightens. The growth rate curve becomes sharper close to the critical latitude, tending to only generate inertial waves (waves at half the primary tide frequency). In fact, at the critical latitude, only one resonant triad exists and both secondary waves have their frequencies equal to $\omega_0/2$. We call this specific TRI, the Parametric Subharmonic Instability (PSI) (Bourget et al., 2013; Bouruet-Aubertot et al., 1995; Staquet & Sommeria, 2002). The sharp increase as $f$ approaches the critical latitude in Figure 2 is not explained by a change in the maximum growth rate, which remains roughly constant with $f$ (crosses in Figure 7b). We now investigate whether the growth rate of the other triad involving waves at $f$ and $\omega_0 - f$ can explain this sharp increase and whether changes in scales of the secondary waves may also play a role, as waves with smaller scales are more prone to break and dissipate their energy.

Figure 8 represents the latitudinal evolution of growth rate, horizontal wave number and vertical wave number for the key frequencies. From the equator toward the critical latitude, we recover the fact that the

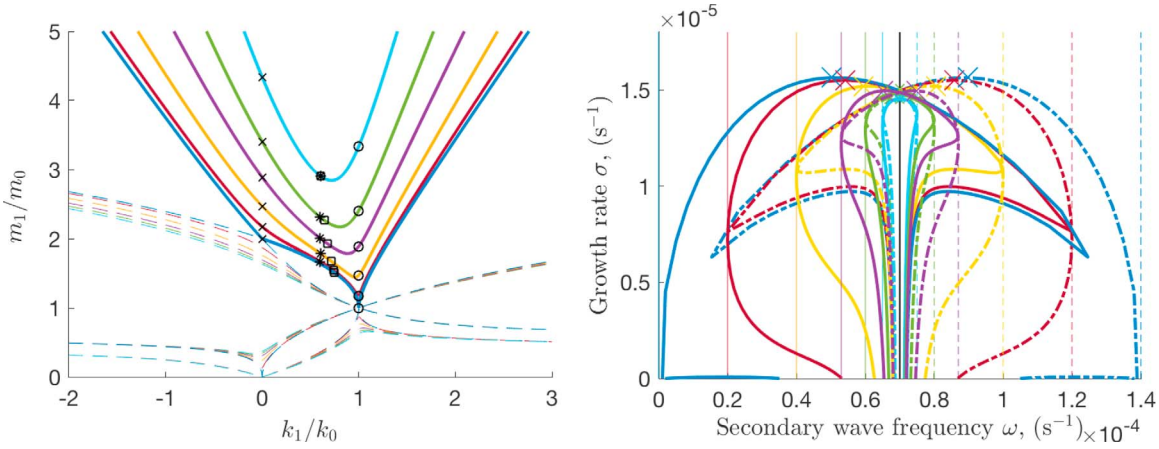


**Figure 7.** (a) Location of ($k_1$, $m_1$) satisfying equation (7) for the three possible combinations of signs for different latitudes. Plain curves are unstable branches and dashed lines are neutral branches. Symbols correspond to ($k_1$, $m_1$) associated with the main frequencies. (b) The associated growth rate as a function of the secondary wave frequencies. Vertical plain lines correspond to $\omega=f$ and vertical dashed lines to $\omega=\omega_0 - f$. Vertical black plain line indicates the critical latitude. Colored cross marks denote maximum growth rate at each latitude.

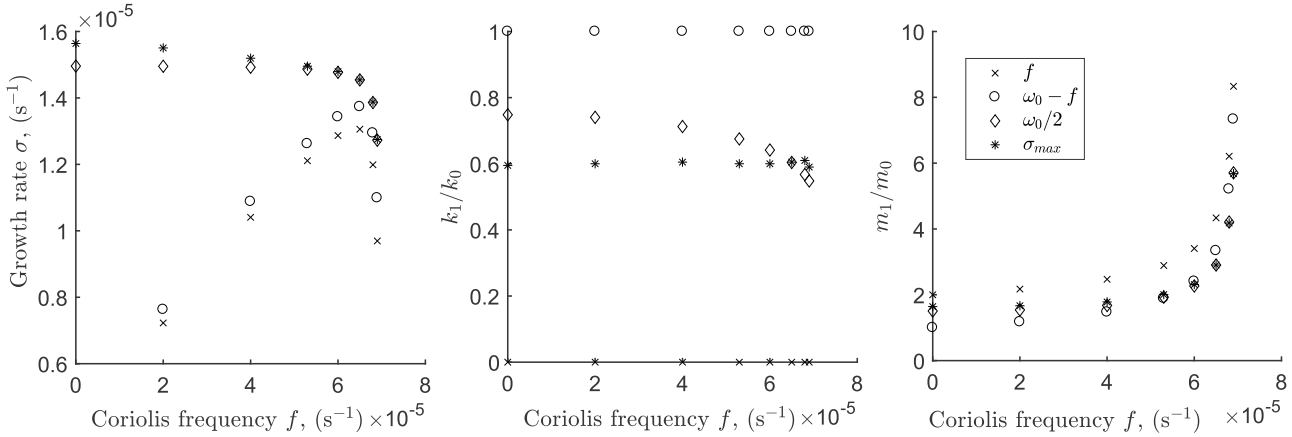


**Figure 8.** Latitudinal evolution of growth rate, horizontal wave number $k_1$, vertical wave number $m_1$ for different frequencies.

maximum growth rate is roughly constant, and even decreases. But the growth rate of inertial waves and waves at $(\omega_0 - f)$ increases. The horizontal scales of the waves seem to be almost constant with latitude. On the other hand, the vertical wave number (vertical scale) increases (decreases) strongly getting closer to the critical latitude. TRIs promote the generation of inertial waves and waves at $\omega_0 - f$ close to the critical latitude, which have smaller and smaller vertical scales near the critical latitude promoting their dissipation. These theoretical results suggest that the enhanced energy dissipation at the critical latitude is due to faster generation (increased growth rate) of secondary waves with smaller vertical scales which are dissipated quickly after their generation, leading to the strong energy dissipation seen in Figure 2.

In the next section, we compare the theoretical results at $f$=0.53×10$^{-4}$ s$^{-1}$ to the numerical simulations for the same latitude.

### 4.2. Numerical Results: Generation of Secondary Waves, Accumulation of Near-Inertial Waves, and Dominant Triad

#### 4.2.1. Stage I: Generation of Secondary Waves

The numerical simulation discussed here is at the same latitude as the theoretical case ($f$=0.53×10$^{-4}$ s$^{-1}$). Several snapshots of the wavefield (left column) and the wavefield without the primary internal tide signal (right column) are shown in Figure 9 at (a) 1.5, (b) 3, (c) 5, and (d) 19 days. The wavefield is obtained by subtracting the zonal mean flow. The primary internal tide has been removed by subtracting two snapshots at $t$ and at $t+T_{tide}$, where $T_{tide}$ is the tide period ($2\pi/\omega_0$~12 h). Linear characteristics for given frequencies are drawn on the snapshots at 5 and 19 days.

The transient phase lasts 3–5 days, corresponding to the development and the propagation of the primary tide toward the sponge layer. As early as 1.5 days of simulation (Figure 9a), waves with smaller wavelengths appear throughout the water depth, faster than expected from upward propagation from topography (the group velocity of small-scale waves is slower than that of large-scale waves). This suggests that they are not generated at the topography during the transient phase, but instead are generated by nonlinearities at all heights. Figures 9a–9c visually confirm that a wide range of secondary waves are generated at the beginning of the simulation by nonlinearities.

Figure 10 shows the time evolution of the kinetic energy of internal waves at $f$, $\omega_0 - f$, at the frequency corresponding to the maximum theoretical growth rate (see Figure 6) and $\omega_0$. The energy of the waves at $\omega_0$ (primary internal tide) remains constant which is coherent with our permanent forcing. For the other frequencies, the kinetic energy grows exponentially in time before reaching nonlinear saturation and equilibrium in 10–20 days. The approximate time scale of energy transfer within the resonant triad, estimated as the $e$-folding time scale from the kinetic energy evolution, is between 1.3 and 2.5 days. These simulated values are in reasonable agreement with the ones found by Nikurashin and Legg (2011) with an approximate time scale of 2–3 days for $\omega_0 - f$. Our numerical growth rates are also broadly consistent with the theoretical estimate of 0.86 days (Figure 6), albeit slightly slower. We interpret this slower simulated time scale as being the consequence of the nonlinear saturation and subsequent slowdown of energy increase visible in Figure 10.

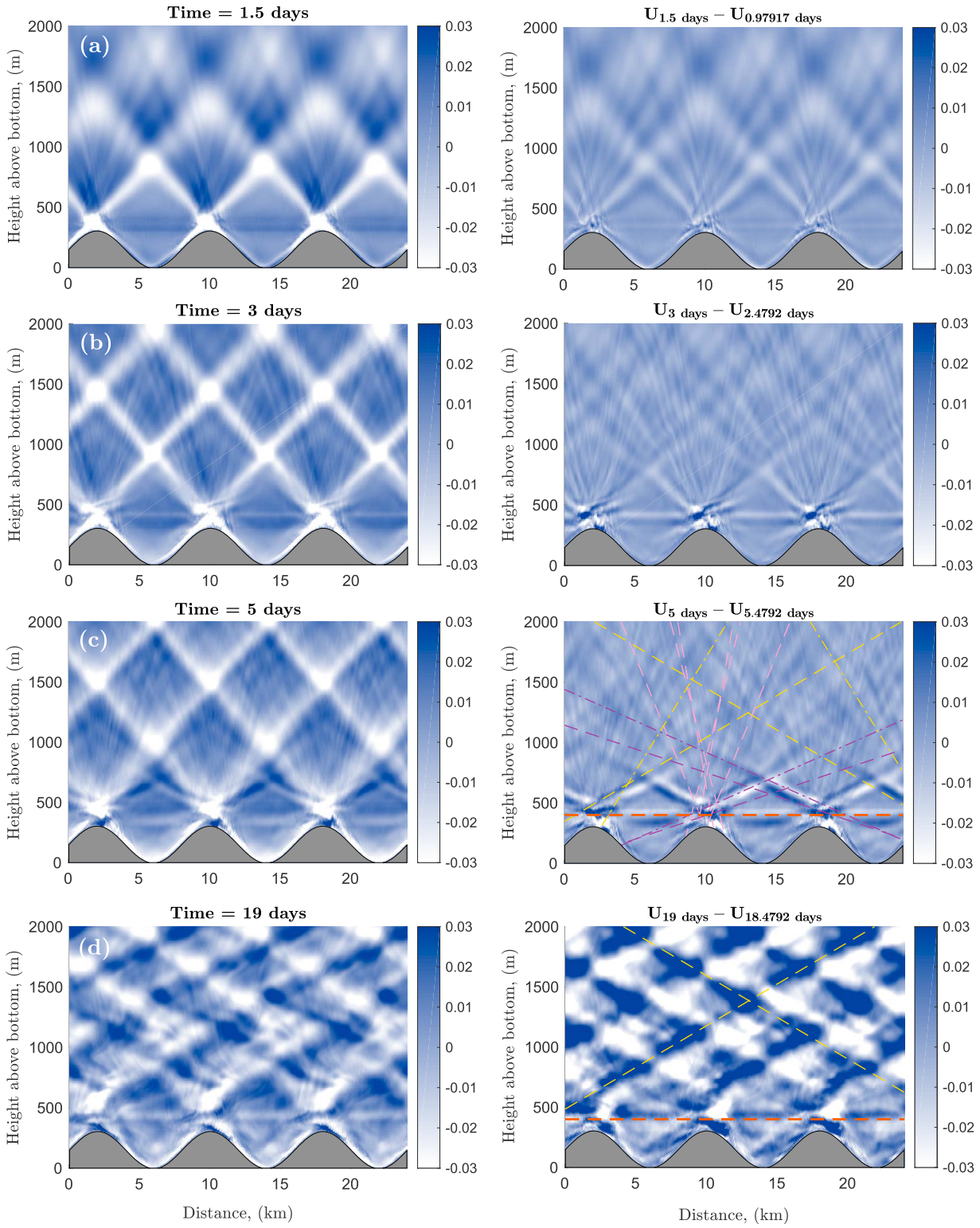


**Figure 9.** Snapshots of (left) the horizontal velocity ($u$, m s$^{-1}$) associated with the wavefield and (right) the wavefield without the primary internal tide signal at (a) 1.5, (b) 3, (c) 5, and (d) 19 days, for $f$=0.53×10$^{-4}$ s$^{-1}$. The wavefield is obtained by subtracting the zonal mean flow. The primary internal tide has been removed by subtracting two snapshots at $t$ and at $t+T_{tide}$, where $T_{tide}$ is the tide period ($2\pi/\omega_0$~12 h). Dashed lines correspond to linear characteristics for waves at $(\omega_0 - f)$ (yellow dashed), $(\omega_0+f)$ (yellow pointed dashed), $\omega_{1,\sigma\max}$ (purple dashed), $\omega_{2,\sigma\max}$ (purple pointed dashed), $f$ (orange dashed), and for harmonics (pink dashed).

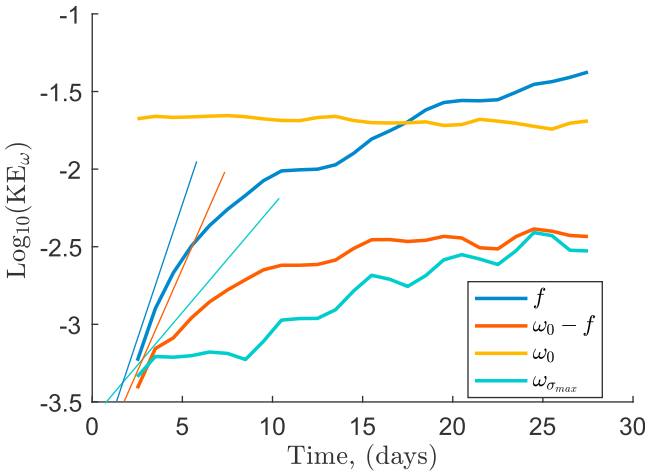


**Figure 10.** Evolution of kinetic energy (in $m^2\ s^{-2}\ cph^{-1}$ with a $\log_{10}$ scale) of internal waves at frequency $f$ (blue), $\omega_0$-$f$ (orange), $\omega_0$ (yellow), and corresponding to the maximum theoretical growth rate (light blue—see Figure 6), computed as an integral of the time spectrum (see Figure 3a) in the frequency range around ±10% of the frequencies on a 5 days window, at $f=0.53\times10^{-4}\ s^{-1}$. Thin lines represent the observed slopes $s$. The associated growth rate is $\sigma=s\log(10)$ which gives for $f$ a growth rate of $\sigma_f=8.9\times10^{-6}\ s^{-1}$ corresponding to a time scale for energy transfer of 1.3 days, for $\omega_0 - f$ a growth rate of $\sigma_{\omega_0-f}=6.8\times10^{-6}\ s^{-1}$ and a time scale of 1.7 days, and for $\omega_{\sigma max}$ a growth rate of $\sigma_{\omega_{\sigma max}}=4.3\times10^{-6}\ s^{-1}$ and a time scale of 2.5 days.

So overall, the simulations show growth rates at early times in good agreement with the theoretical expectations. Furthermore, we see that all triads exhibit similar rates of increase, consistent with the flat theoretical growth rate curves in Figure 6 (similar growth rate for all frequencies), and consistent with the wide range of wave frequencies generated at early times in the simulations (as can be seen with the wide range of wave slopes in Figure 9c).

#### 4.2.2. Stage II: Accumulation of Near-Inertial Waves

Figure 11 shows the kinetic energy associated with the different frequencies in the simulation over the period 1–15 days and 15–30 days. During the first 15 days, the most energetic waves are associated with frequencies $\omega_0$, the primary internal tide, $f$, the near-inertial wave and $\omega_0 - f$. There is a signal at $\omega = 0\ s^{-1}$, probably linked to a weak mean flow induced by the waves (Grisouard & Bühler, 2012). During the second period, near-inertial waves have more and more energy and become stronger than the primary internal wave. The near-inertial waves are present above topography until 2,500 m, and have significant energy as high as 1,500 m above the bottom.

Near-inertial waves (i.e., with frequencies near $f$) are those with vertical group velocity close to zero (in fact for inertial waves $\omega=f$, $k_{IW}=0$ $\Rightarrow c_{g,z}=\partial\omega/\partial m=0$ and for this reason, they do not propagate, consistent with the horizontal waves at the topography for instance, Figure 9d). In the simulation, the magnitude of the vertical group velocity of the near-inertial wave is of the order of $10^{-6}$ m $s^{-1}$ (for comparison the magnitude of the vertical group velocity for the waves at $\omega_0 - f$ is ~$10^{-3}$ m $s^{-1}$). For this reason, gradually, they accumulate near their generation site, growing to order one and cannot be considered as noise anymore compared to the primary internal wave.

The sign of the vertical group velocity of internal waves,

$$Cg_z = -\frac{mk^2(N^2 - f^2)}{\omega(k^2+m^2)^2}, \tag{9}$$

is minus the sign of the vertical wave number $m$ ($\omega$ is positive with our convention). Figure 12 shows the kinetic energy of the waves as a function of vertical wave number and frequency over 1–15 days and 15–30 days. As seen previously, near-inertial waves have more and more energy. The near-inertial waves are associated with a vertical wave number positive which means that the energy goes toward the topography and confirm the accumulation of near-inertial waves at the topography. After 15 days, near-inertial waves and primary internal tide are of the same order.

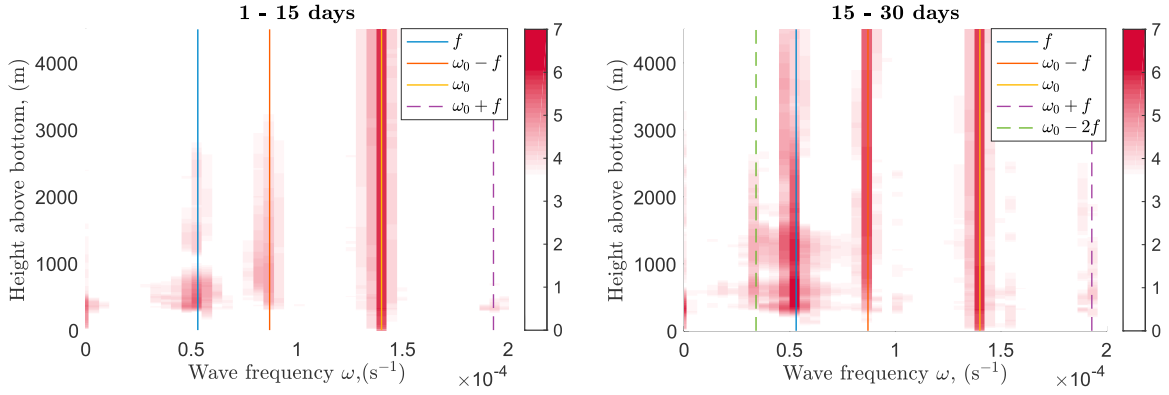


**Figure 11.** Kinetic energy spectrum in time (in $m^2\ s^{-2}$ with a $\log_{10}$ scale) as a function of wave frequency $\omega$ and height above topography, and averaged zonally over the time period of (left) 1–15 days and (right) 15–30 days, for $f=0.53\times10^{-4}\ s^{-1}$. Vertical lines correspond to the main observed frequencies.

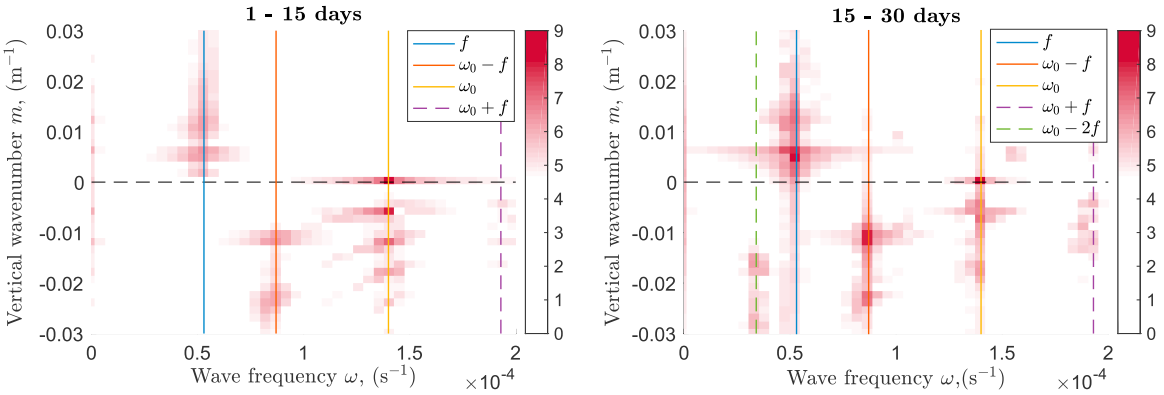


**Figure 12.** Kinetic energy spectrum in time and space (in m$^2$ s$^{-2}$ with a log$_{10}$ scale) as a function of wave frequency $\omega$ and vertical wave number $m$, and averaged zonally over the time period of (right) 1–15 days and (left) 15–30 days, for $f$=0.53×10$^{-4}$ s$^{-1}$. Vertical lines corresponds to the main observed frequencies.

#### 4.2.3. Stage III: Dominant TRI

Consistent with the aforementioned accumulation of inertial waves, the wavefield in the numerical simulation strongly evolves with time and the waves are very different after 19 days compared to earlier times (see Figure 9d right plot, where the primary internal tide has been removed). The linear characteristics highlight the waves at frequency $(\omega_0 - f)$ which dominate in the whole domain at the end of the simulation. The triad with waves at $f$ and $\omega_0 - f$ has become order one and clearly dominates the wavefield.

In fact, if we come back to Figures 11 and 12, we can see that waves at $\omega_0 - f$ have more and more energy over time suggesting that their generation is linked to the strengthening of the near-inertial waves. Figure 12 also shows that waves at $\omega_0 - f$ have a vertical wave number $m < 0$ implying that they propagate upward and their energy, not dissipated locally, is dissipated in the sponge layer. This result is coherent with Figure 11 where $\omega_0 - f$ has homogeneous kinetic energy all over the water column above the maximum of $f$.

Going back to the TRI theory and triad selection, Figure 12 gives one more information which is that the selected triad is the triad $(\omega_1{=}\omega_0 - f, m_1 < 0)$ and $(\omega_2{=}f, m_2 > 0)$. This triad is located on the right part of the upper unstable branch (see Figure 5 as well as Figure 7a). Indeed, $m_1 < 0$ (same sign as $m_0$ on this branch), thus the triad selected corresponds to $\omega_1{=}\omega_0 - f$ with $m_1 < 0$, open circles on Figure 7. Note that in that case $m_2 > 0$ (since $|m_1/m_0| > 1$ see Figure 7) and the wave $\omega_2{=}f$, $m_2 > 0$ thus propagates downward consistent with Figure 12 and the aforementioned accumulation of inertial waves at the topography.

The increase of energy in near-inertial waves, becoming order one compared to the primary tide, forces the triad composed by the primary tide at $\omega_0$, the near-inertial at $f$ and a third wave to grow. The third wave frequency could be, with the combination of $\omega_0$ and $f$, $(\omega_0 - f)$ or $(\omega_0{+}f)$. If we go back to the triadic relation (equation (7)), the only unstable branch corresponds to sign combination $(s_1{=}+, s_2{=}+)$, yielding $\omega_0{=}\omega_1{+}\omega_2$, with $\omega_{0,1,2}$ positive. This result implies that the only unstable triad is between frequencies $\omega_0$, $f$ and $\omega_0 - f$. In other words, the dominant TRI generates waves at frequency $(\omega_0 - f)$. This theoretical result is confirmed by the numerical simulation in Figure 9d.

Thus, we conclude that in our simulations, equatorward of the critical latitude, the dissipation of internal tides involves energy transfers to smaller scales (smaller frequencies) via TRI. More precisely, it occurs in three stages: generation of new secondary waves via TRIs over a wide range of frequencies, accumulation of inertial waves which cannot propagate vertically, and domination of a TRI between the primary internal tide and inertial waves involving a third wave at $\omega_0 - f$. This theoretical and numerical study of internal tide instability and dissipation confirms the prediction that TRI is the main mechanism for internal tide dissipation in the ocean. We note that in the ocean, assuming that a steady state with the barotropic tidal forcing is reached, stages I and II are not relevant, and it is stage III, i.e., the strengthening of the dominant triad due to the order one inertial waves, which dominates.

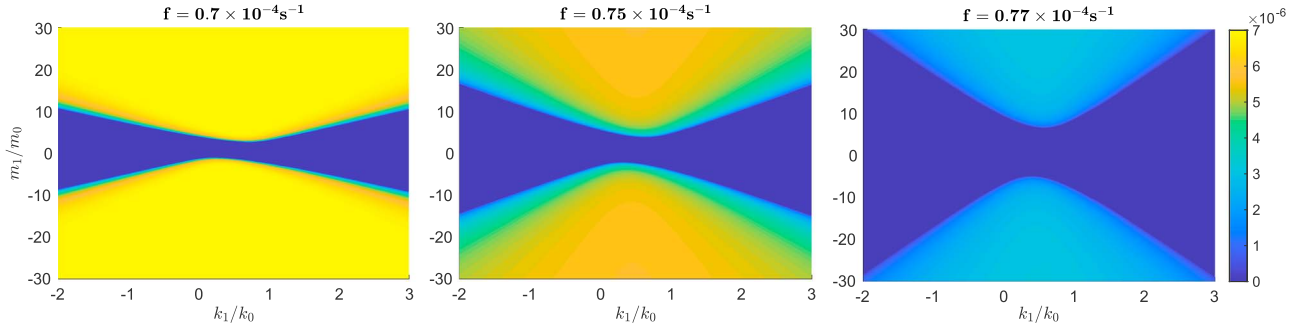


**Figure 13.** Growth rate (in $s^{-1}$) from (12) as a function of $m_1/m_0$ and $k_1/k_0$ for different latitudes: $f$=0.7×10$^{-4}$ $s^{-1}$, $f$=0.75×10$^{-4}$ $s^{-1}$, and $f$=0.77×10$^{-4}$ $s^{-1}$.

## 5. Part II—Poleward of the Critical Latitude: Evanescent Waves

Poleward of the critical latitude, TRI is not a possible mechanism for internal tide dissipation, since waves at $\omega_0 - f$ are not radiating internal waves anymore (see equation (4), the range of frequencies of propagating internal waves is between $f$ and $N$). But surprisingly, the dissipation does not decrease sharply. Instead, internal tides continue to dissipate for about 5° of latitude poleward (see Figure 2) and thus to participate in diapycnal mixing. The energy dissipation seems to be associated with waves at $\omega_0/2$ (see Figure 4) which are not radiating either ($\omega_0/2 < f$), but instead are evanescent. Young et al. (2008) propose a mechanism, the "2$f$-pump," which extends PSI theory poleward of the critical latitude. In Young et al.'s (2008) theory, the barotropic tide at $\omega_0$ is able to exchange energy with near-inertial waves, leading to its dissipation. Here we compare expectations from this theory to our simulations.

### 5.1. Theory of PSI Extension

In Young et al.'s (2008) theory, internal tides can transfer energy to evanescent secondary waves at $\omega_0/2$ via a mechanism called the 2$f$-pump. As mentioned earlier, we refer to PSI as the specific TRI where resonant conditions are

$$\mathbf{k_0}=\mathbf{k_1}+\mathbf{k_2}, \tag{10}$$

$$\omega_0=\omega_1+\omega_2=\frac{\omega_0}{2}+\frac{\omega_0}{2}. \tag{11}$$

Young et al. (2008) studied near-inertial PSI which corresponds to a case where the primary wave has a frequency $\omega_0 \approx 2f$, where $f$ is the local inertial frequency, inducing that secondary waves are near-inertial oscillations. Transfer of energy in this mechanism is particularly efficient because near-inertial oscillations are almost stationary and therefore might dissipate locally.

Young et al. (2008) show that an infinite-plane wave at frequency $\omega_0=2f+\varepsilon$, ($\varepsilon \ll f$ and $\varepsilon$ can be positive or negative), extracts energy from the nongeostrophic part of the background flow then transferring to near-inertial oscillations via near-inertial PSI. If the detuning frequency $\varepsilon$ is negative, which means secondary waves at $\omega_0/2$ fall outside the internal wave frequency band [$f$, $N$], Young et al. (2008) point that PSI can extend the internal wave frequency band to slightly subinertial frequencies.

The growth rate of the near-inertial PSI of an infinite-plane internal wave $\omega_0=2f+\varepsilon$, on the $f$-plane, is:

$$\sigma=\frac{1}{2}\sqrt{\lambda^2-\left(\frac{N^2}{2f}\right)^2\left(\frac{k_1^2}{m_1^2}+\frac{k_2^2}{m_2^2}-2\frac{\varepsilon f}{N^2}\right)^2}, \tag{12}$$

where

$$\lambda^2=\frac{U_0 h_0 k_0^2}{2\omega_0}\sqrt{\frac{(N^2-\omega_0^2)(\omega_0+f)}{(\omega_0-f)}}, \tag{13}$$

see Appendix B for the full growth rate calculation and e.g., Muller and Buhler (2009) for polarization relations (their equation (9)) used to determine the amplitude of the 2$f$-pump in our simulations.

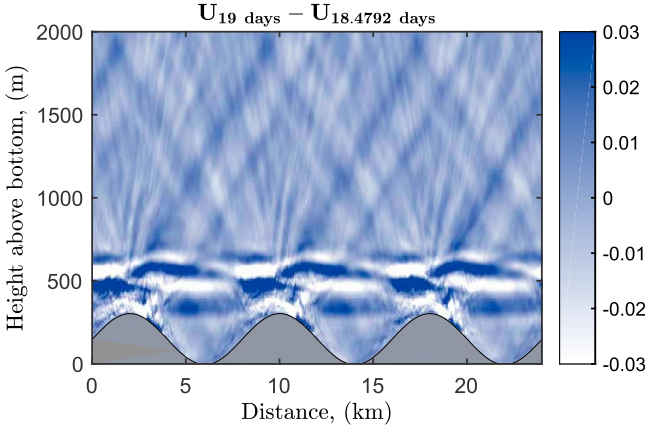


**Figure 14.** Snapshot of the wavefield after removing the primary internal tide at 5 days, for $f=0.75\times10^{-4}$ s$^{-1}$. The wavefield is obtained by subtracting the zonal mean flow.

Figure 13 represents the growth rate from equation (12) for different latitudes. The growth rate of near-inertial PSI is maximum at the critical latitude ($f=0.7\times10^{-4}$ s$^{-1}$) and decreases poleward of the critical latitude. A second important point is that the instability is larger at higher vertical wave number (small vertical scales). This last result is consistent with the strong dissipation observed near and poleward of the critical latitude (see Figure 2), since dissipation is favored by smaller-scale waves. When $m_1/m_0\to\infty$, the growth rate asymptotes to $\frac{1}{2}\sqrt{\lambda^2-\varepsilon^2}$. From this result, we can evaluate $\varepsilon_c$ when the growth rate is zero. We obtain $\varepsilon_c/f\approx0.2$ which extends the dissipation poleward of the critical latitude to $f\approx0.77\times10^{-4}$ s$^{-1}$ (~32°). This result is in excellent quantitative agreement with the latitudinal extent of enhanced dissipation poleward of the critical latitude found in our simulations (Figure 2). Further comparison with our numerical results are provided in the next section.

### 5.2. Numerical Results

Figure 14 is a snapshot of the wavefield at 19 days (primary internal tide removed) for a simulation poleward of the critical latitude ($f=0.75\times10^{-4}$ s$^{-1}$). The near-inertial waves are confined to a few hundred meters from topography, as expected since those waves are not propagating (frequency lower than $f$).

The time evolution of kinetic energy at $\omega_0$ and $\omega_0/2$ at $f=0.75\times10^{-4}$ s$^{-1}$ is shown in Figure 15. As we have seen previous for the time evolution of kinetic energy for $f=0.53\times10^{-4}$ s$^{-1}$ (Figure 10), the energy remains globally constant at $\omega_0$ due to the constant generation of the primary tide. For the waves at $\omega_0/2$, the kinetic energy grows exponentially in time reaching the equilibrium after the first 10–20 days of simulation. The energy transfer at $\omega_0/2$ has a time scale of 1.4 days which is in good agreement with the theoretical time scale of energy transfer of 2 days, obtained from Figure 13.

Consistent with Figure 2 and with the theoretical latitude of zero growth rate derived at the end of the previous section, we find that those near-inertial waves at $\omega_0/2$ are present approximately until $f=0.8\times10^{-4}$ s$^{-1}$. These results suggest that poleward of the critical latitude, the dissipation of internal tides is dominated by this extension of PSI, namely the 2$f$-pump mechanism. In other words, we find that the generation of evanescent waves via nonlinear energy transfers from the primary internal tide, is an efficient process to dissipate tidal energy.

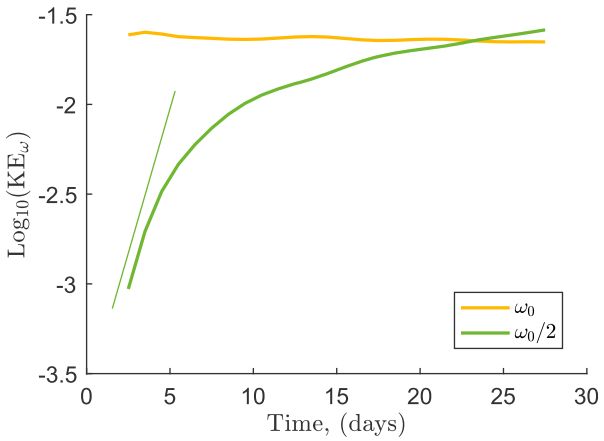


**Figure 15.** Evolution of kinetic energy (in m$^2$ s$^{-2}$ cph$^{-1}$ with a $\log_{10}$ scale) of internal waves at frequency $\omega_0$ (yellow) and $\omega_0/2$ (green), computed as an integral of the time spectrum (see Figure 3b) in the frequency range around ±10% of the frequencies on a 5 days window, at $f=0.75\times10^{-4}$ s$^{-1}$. Thin line represents the observed slopes $s$. The associated growth rate is $\sigma=s\log(10)$ which corresponds for $\omega_0/2$ to a growth rate of $\sigma_{\omega_0/2}=3.7\times10^{-6}$ s$^{-1}$ and a time scale of energy transfer of 1.4 days.

Though PSI has been widely studied, the transfer of energy to evanescent waves has not received as much attention, while our work suggests that it could be an equally efficient mechanism to dissipate tidal energy near the critical latitude.

## 6. Discussion and Conclusions

In this paper, we investigate the physical processes responsible for the dissipation of internal tides. In particular, we want to determine which physical process, if any, dominates in setting the latitudinal distribution of tidal dissipation and the strong enhancement of energy dissipation at the critical latitude $f\approx0.7\times10^{-4}$ s$^{-1}$ (Figure 2). Our results suggest that the physical process behind the dissipation of internal tides is different equatorward and poleward of the critical latitude.

Equatorward of the critical latitude, triadic resonant instabilities (TRI) are the most efficient mechanism to transfer energy from the primary wave, i.e., the internal tide, to secondary waves. These secondary waves have lower frequencies than the primary wave, hence smaller vertical scales, and are more prone to dissipate. In our simulations, this mechanism involves three stages after the generation of the primary internal tide.

The two first stages correspond to the generation of secondary waves at various frequencies with a time scale for energy transfer on the order of a few days via TRI, and then the accumulation of near-inertial waves close to the topography because of their small vertical group velocity. Note that it is interesting that near-inertial waves have a nonzero vertical group velocity permitting a slow propagation upward or downward. In the numerical simulations, the dominant triad has a downward propagating near-inertial wave and an upward-propagating wave at $\omega_0 - f$. The selection of the direction of propagation for the secondary waves is not explained by the TRI theory which predicts the generation of both triads and this observation in the simulation remains unclear. The third stage corresponds to the moment where inertial waves become of the same order as the primary internal tide, and the triadic interaction between the primary wave at $\omega_0$ and inertial waves at $f$ leads to the strengthening of waves at $\omega_0 - f$. This mechanism leads to the dominant resonant triad composed by $\omega_0$, $f$ and $\omega_0 - f$ as proposed by Nikurashin and Legg (2011). In the ocean only the last stage is relevant, if we consider that the ocean has reached a steady state. Internal tides and inertial waves are of the same order, and they interact nonlinearly to generate waves at $\omega_0 - f$. TRI is found to be a powerful mechanism to extract tidal energy. The increase of energy dissipation from the equator toward the critical latitude is due to increased instability growth rates, as well as to the smaller and smaller vertical scales of the secondary waves (Figure 8), hence more likely to break and dissipate their energy.

Poleward of the critical latitude, the "2*f*-pump" mechanism described in Young et al. (2008) seems to be the leading-order mechanism by which internal tides lose energy. In this case, the internal tide transfers energy nonlinearly to evanescent waves at frequencies $\omega_0/2$, which dissipate internal tide energy as efficiently as PSI equatorward of the critical latitude. In fact, the 2*f*-pump is an extension of PSI poleward of the critical latitude when we consider near-inertial waves ($f+\varepsilon$) for small values of $\varepsilon$. The dissipation poleward of the critical latitude has implications for the possible consumption of AABW. These results suggest that evanescent waves could play a leading-order role in the dissipation of tidal energy in the deep ocean poleward of the critical latitude, and could contribute significantly to the diapycnal mixing relevant to the large-scale ocean circulation and to water masses.

## Appendix A: Growth Rate Calculations

In this section, we develop the full growth rate calculation for a triadic resonant instability in a rotating frame, following Bourget et al. (2013) and Maurer et al. (2016).

Using equations (1), (2), and (3), and introducing the stream function $\psi$ with $\mathbf{u}=(\partial_z\psi, v, -\partial_x\psi)$ (recall that the velocity $v$ is constant in our setting), we obtain a new set of equations

$$\frac{\partial\nabla^2\psi}{\partial t}+J(\nabla^2\psi,\psi)-f\frac{\partial v}{\partial z}=-\frac{\partial b}{\partial x}+\nu\Delta^2\psi, \tag{A1}$$

$$\frac{\partial v}{\partial t}+J(v,\psi)+f\frac{\partial\psi}{\partial z}=\nu\Delta v, \tag{A2}$$

$$\frac{\partial b}{\partial t}+J(b,\psi)=N^2\frac{\partial\psi}{\partial x}, \tag{A3}$$

where $J$ is the Jacobian operator such as $J(A,B)=\partial_x A\partial_z B-\partial_z A\partial_x B$. We are interested in triadic interactions, so we are looking for solutions of the form

$$\psi=\sum_{j=0}^{2}\Psi_j(t)e^{i(\mathbf{k_j}\cdot\mathbf{r}-\omega_j t)}+c.c., \tag{A4}$$

$$v=\sum_{j=0}^{2}V_j(t)e^{i(\mathbf{k_j}\cdot\mathbf{r}-\omega_j t)}+c.c., \tag{A5}$$

$$b=\sum_{j=0}^{2}R_j(t)e^{i(\mathbf{k_j}\cdot\mathbf{r}-\omega_j t)}+c.c., \tag{A6}$$

where $\mathbf{k_j}=(k,0,m)$ is the wave vector. Using these solutions in equations (A1), (A2), and (A3), we obtain

$$\sum_{j=0}^{2}[-\kappa_j^2(\dot{\Psi}_j - i\omega_j\Psi_j)+ik_jR_j - \nu\kappa_j^4\Psi_j - ifm_jV_j]e^{i(\mathbf{k_j}\cdot\mathbf{r}-\omega_j t)}+c.c.=-J(\Delta\psi,\psi), \tag{A7}$$

$$\sum_{j=0}^{2}[\dot{V}_j - i\omega_jV_j+\nu\kappa_j^2V_j+ifm_j\Psi_j]e^{i(\mathbf{k_j}\cdot\mathbf{r}-\omega_j t)}+c.c.=-J(v,\psi), \tag{A8}$$

$$\sum_{j=0}^{2}[\dot{R}_j - i\omega_jR_j - iN^2k_j\Psi_j]e^{i(\mathbf{k_j}\cdot\mathbf{r}-\omega_j t)}+c.c.=-J(b,\psi), \tag{A9}$$

where $\kappa_j=\sqrt{k_j^2+m_j^2}$. The Jacobian terms on the right-hand side can be rearranged. The usual inviscid linear dynamics of (A8) and (A9) provides the polarization relation

$$R_j=-\frac{N^2k_j}{\omega_j}\Psi_j, \tag{A10}$$

$$V_j=\frac{fm_j}{\omega_j}\Psi_j. \tag{A11}$$

After some calculations on equations (A7), (A8), and (A9), they become

$$\begin{aligned}J(\Delta\psi,\psi)=&\sum_{p=0}^{2}\sum_{q\neq p}[(k_pm_q-m_pk_q)\kappa_p^2\Psi_p\Psi_q]e^{i[(\mathbf{k_p}+\mathbf{k_q})\cdot\mathbf{r}-(\omega_p+\omega_q)t]}\\&-[(k_pm_q-m_pk_q)\kappa_p^2\Psi_p\Psi_q^\star e^{i[(\mathbf{k_p}-\mathbf{k_q})\cdot\mathbf{r}-(\omega_p-\omega_q)t]}]+c.c.\end{aligned} \tag{A12}$$

$$\begin{aligned}J(v,\psi)=&\sum_{p=0}^{2}\sum_{q\neq p}[(-k_pm_q+m_pk_q)V_p\Psi_q]e^{i[(\mathbf{k_p}+\mathbf{k_q})\cdot\mathbf{r}-(\omega_p+\omega_q)t]}\\&-[(-k_pm_q+m_pk_q)V_p\Psi_q^\star e^{i[(\mathbf{k_p}-\mathbf{k_q})\cdot\mathbf{r}-(\omega_p-\omega_q)t]}]+c.c.\end{aligned} \tag{A13}$$

$$\begin{aligned}J(b,\psi)=&\sum_{p=0}^{2}\sum_{q\neq p}[(k_pm_q-m_pk_q)R_p\Psi_q]e^{i[(\mathbf{k_p}+\mathbf{k_q})\cdot\mathbf{r}-(\omega_p+\omega_q)t]}\\&-[(-k_pm_q+m_pk_q)R_p\Psi_q^\star e^{i[(\mathbf{k_p}-\mathbf{k_q})\cdot\mathbf{r}-(\omega_p-\omega_q)t]}]+c.c.\end{aligned} \tag{A14}$$

We now get the evolution of a particular wave number component $(\mathbf{k_r},\omega_r)$ associated with the stream function $\psi$, in which $r=0$, 1 or 2, by averaging both the left-hand and the right-hand side over the period of that wave. The resonant terms on the right-hand side that balance the left-hand side correspond to the wave fulfilling the resonant conditions 5 and 6.

Highlighting only the resonant terms and using the polarization relations (A10) and (A11), the Jacobian terms can be rewritten as

$$\begin{aligned}J(\nabla^2\psi,\psi)=&(k_1m_2-m_1k_2)(\kappa_1^2-\kappa_2^2)\Psi_1\Psi_2e^{i(\mathbf{k_0}\cdot\mathbf{r}-\omega_0t)}\\&-(k_0m_2-m_0k_2)(\kappa_0^2-\kappa_2^2)\Psi_0\Psi_2^\star e^{i(\mathbf{k_1}\cdot\mathbf{r}-\omega_1t)}\\&-(k_0m_1-m_0k_1)(\kappa_0^2-\kappa_1^2)\Psi_0\Psi_1^\star e^{i(\mathbf{k_2}\cdot\mathbf{r}-\omega_2t)}+NRT,\end{aligned} \tag{A15}$$

$$\begin{aligned}J(v,\psi)=&-(k_1m_2-m_1k_2)f\left(\frac{m_1}{\omega_1}-\frac{m_2}{\omega_2}\right)\Psi_1\Psi_2e^{i(\mathbf{k_0}\cdot\mathbf{r}-\omega_0t)}\\&+(k_0m_2-m_0k_2)f\left(\frac{m_0}{\omega_0}-\frac{m_2}{\omega_2}\right)\Psi_0\Psi_2^\star e^{i(\mathbf{k_1}\cdot\mathbf{r}-\omega_1t)}\\&+(k_0m_1-m_0k_1)f\left(\frac{m_0}{\omega_0}-\frac{m_1}{\omega_1}\right)\Psi_0\Psi_1^\star e^{i(\mathbf{k_2}\cdot\mathbf{r}-\omega_2t)}+NRT,\end{aligned} \tag{A16}$$

$$J(b,\psi)=(k_1m_2-m_1k_2)N^2\left(\frac{k_1}{\omega_1}-\frac{k_2}{\omega_2}\right)\Psi_1\Psi_2e^{i(\mathbf{k_0}\cdot\mathbf{r}-\omega_0t)}$$
$$-(k_0m_2-m_0k_2)N^2\left(\frac{k_0}{\omega_0}-\frac{k_2}{\omega_2}\right)\Psi_0\Psi_2^\star e^{i(\mathbf{k_1}\cdot\mathbf{r}-\omega_1t)} \quad \text{(A17)}$$
$$-(k_0m_1-m_0k_1)N^2\left(\frac{k_0}{\omega_0}-\frac{k_1}{\omega_1}\right)\Psi_0\Psi_1^\star e^{i(\mathbf{k_2}\cdot\mathbf{r}-\omega_2t)}+NRT,$$

where NRT is the acronym for nonresonant terms and they are not relevant for this problem.

At the first order, we make the further assumption that the amplitude $\Psi_j$ varies slowly with respect to the period of the wave. It is therefore appropriate to consider that $\dot{\Psi}_j \ll \omega_j\Psi_j$. Use of this assumption in the derivative of (A10) and (A11) yields

$$\dot{V}_j=\frac{fm_j}{\omega_j}\dot{\Psi}_j, \quad \text{(A18)}$$

$$\dot{R}_j=-\frac{N^2k_j}{\omega_j}\dot{\Psi}_j. \quad \text{(A19)}$$

Using (A18) in resonant terms of equation (A8), we obtain

$$V_0=\frac{-\gamma_0\beta_0\Psi_1\Psi_2+ifm_0\Psi_0+f\frac{m_0}{\omega_0}\partial_t\Psi_0}{i\omega_0-\nu\kappa_0^2}, \quad \text{(A20)}$$

$$V_1=\frac{-\gamma_1\beta_1\Psi_0\Psi_2^\star+ifm_1\Psi_1+f\frac{m_1}{\omega_1}\partial_t\Psi_1}{i\omega_1-\nu\kappa_1^2}, \quad \text{(A21)}$$

$$V_2=\frac{-\gamma_2\beta_2\Psi_0\Psi_1^\star+ifm_2\Psi_2+f\frac{m_2}{\omega_2}\partial_t\Psi_2}{i\omega_2-\nu\kappa_2^2}, \quad \text{(A22)}$$

where $\gamma_0=1$, $\gamma_{1,2}=-1$ and

$$\beta_r=(k_pm_q-m_pk_q)\left(\frac{m_p}{\omega_p}-\frac{m_q}{\omega_q}\right), \quad \text{(A23)}$$

with $(p,q,r)=(0,1,2)$ or any circular permutation. Now, using (A19) in resonant terms of equation (A7)

$$R_0=-\frac{i}{k_0}\left[\kappa_0^2(\dot{\Psi}_0-i\omega_0\Psi_0)+\nu\kappa_0^4\Psi_0-\gamma_0\alpha_0\Psi_1\Psi_2+ifm_0V_0\right], \quad \text{(A24)}$$

$$R_1=-\frac{i}{k_1}\left[\kappa_1^2(\dot{\Psi}_1-i\omega_1\Psi_1)+\nu\kappa_1^4\Psi_1-\gamma_1\alpha_1\Psi_0\Psi_2^\star+ifm_1V_1\right], \quad \text{(A25)}$$

$$R_2=-\frac{i}{k_2}\left[\kappa_2^2(\dot{\Psi}_2-i\omega_2\Psi_2)+\nu\kappa_2^4\Psi_2-\gamma_2\alpha_2\Psi_0\Psi_1^\star+ifm_2V_2\right], \quad \text{(A26)}$$

where

$$\alpha_r=(k_pm_q-m_pk_q)(\kappa_p^2-\kappa_q^2), \quad \text{(A27)}$$

with $(p,q,r)=(0,1,2)$ or any circular permutation. Therefore, using all the previous results in equation (A9) leads to

$$\frac{N^2k_0}{\omega_0}\dot{\Psi}_0+i\omega_0R_0+iN^2k_0\Psi_0=\gamma_0\delta_0N^2\Psi_1\Psi_2, \quad \text{(A28)}$$

where

$$\delta_r=(k_pm_q-m_pk_q)\left(\frac{k_p}{\omega_p}-\frac{k_q}{\omega_q}\right), \quad \text{(A29)}$$

with $(p,q,r)=(0,1,2)$ or any circular permutation. Replacing $R_0$ and $V_0$ by their expression

$$\frac{N^2k_0^2}{\omega_0^2\dot{\Psi}_0}+\kappa_0^2(\dot{\Psi}_0-i\omega_0\Psi_0)+\nu\kappa_0^4\Psi_0-\gamma_0\alpha_0\Psi_1\Psi_2 +ifm_0\left(\frac{-\gamma_0 f\beta_0\Psi_1\Psi_2+ifm_0\Psi_0+f\frac{m_0}{\omega_0}\dot{\Psi}_0}{i\omega_0-\nu\kappa_0^2}\right)+i\frac{N^2k_0}{\omega_0}\Psi_0=\gamma_0\frac{k_0}{\omega_0}\delta_0N^2\Psi_1\Psi_2, \tag{A30}$$

relating the time derivative of the wave amplitude, $\Psi_0$, to the other wave amplitudes.

$$\dot{\Psi}_0=\frac{\gamma_0}{2\kappa_0^2}\left(\alpha_0+\frac{\delta_0N^2k_0}{\omega_0}+\frac{f^2m_0\beta_0}{\omega_0}\right)\Psi_1\Psi_2-\frac{1}{2}\nu\left(\kappa_0^2+\frac{f^2m_0^2}{\omega_0^2}\right)\Psi_0. \tag{A31}$$

$$\dot{\Psi}_0=I_0\Psi_1\Psi_2-\frac{1}{2}\nu\kappa_0^2\left(1+\frac{f^2m_0^2}{\kappa_0^2\omega_0^2}\right)\Psi_0, \tag{A32}$$

$$\dot{\Psi}_1=I_1\Psi_0\Psi_2^\star-\frac{1}{2}\nu\kappa_1^2\left(1+\frac{f^2m_1^2}{\kappa_1^2\omega_1^2}\right)\Psi_1, \tag{A33}$$

$$\dot{\Psi}_2=I_2\Psi_0\Psi_1^\star-\frac{1}{2}\nu\kappa_2^2\left(1+\frac{f^2m_2^2}{\kappa_2^2\omega_2^2}\right)\Psi_2, \tag{A34}$$

where $I_r$ is

$$I_r=\frac{\gamma_r}{2\kappa_r^2}\left(\alpha_r+\frac{\delta_rN^2k_r}{\omega_r}+\frac{f^2m_r\beta_r}{\omega_r}\right) =\gamma_r\frac{k_pm_q-m_pk_q}{2\omega_r\kappa_r^2}\left[\omega_r(\kappa_p^2-\kappa_q^2)+k_rN^2\left(\frac{k_p}{\omega_p}-\frac{k_q}{\omega_q}\right)+m_rf^2\left(\frac{m_p}{\omega_p}-\frac{m_q}{\omega_q}\right)\right]. \tag{A35}$$

We consider $\Psi_0$ as the primary wave and it is constant in early times since amplitudes of the secondary waves, $\Psi_1$ and $\Psi_2$ are negligible compare to the amplitude of $\Psi_0$. Combining equations (A33) and (A34), we get

$$\ddot{\Psi}_1=I_1I_2\Psi_0^2\Psi_1-\frac{1}{4}\nu^2\kappa_1^2\kappa_2^2\left(1+\frac{f^2m_1^2}{\kappa_1^2\omega_1^2}\right)\left(1+\frac{f^2m_2^2}{\kappa_2^2\omega_2^2}\right)\Psi_1-\frac{1}{2}\nu\left(\kappa_1^2+\kappa_2^2+\frac{f^2m_1^2}{\omega_1^2}+\frac{f^2m_2^2}{\omega_2^2}\right)\dot{\Psi}_1. \tag{A36}$$

The solution of equation (A36) is of the form $\Psi_{1,2}=A_{1,2}e^{\sigma_+T}+B_{1,2}e^{\sigma_-T}$, where $\sigma$ is the growth rate defined as (8).

## Appendix B: PSI Extension Calculations

In this part, we give a brief description of the 2*f*-pump mechanism described in detail in Young et al. (2008). Of particular interest is the derivation of the growth rate (equation (12)). We consider the interaction of a background flow (*U*, *V*, *W*) with a pure inertial oscillation. *W* is a function of time *t* and depth *z* and is given by the incompressibility condition $U_x+V_y+W_z=0$. For us, a pure inertial oscillation is a disturbance with infinite horizontal spatial scales which implicates that the velocity is $(u(z,t),v(z,t),0)$. A pure inertial oscillation has no pressure or buoyancy signal so that its dynamic is entirely governed by the horizontal momentum equations, after removing second order terms,

$$u_t+Wu_z+uU_x+vU_y-fv=0, \tag{B1}$$

$$v_t+Wv_z+uV_x+vV_y+fu=0. \tag{B2}$$

Rewriting equations (B1) and (B2) in term of the "back-rotated" velocity $\Omega\equiv(u+iv)e^{ift}$, we obtain

$$\Omega_t+W\Omega_z+\frac{1}{2}\left[(U_x+V_y)+i(V_x-U_y)\right]\Omega+\frac{1}{2}\left[(U_x-V_y)+i(V_x+U_y)\right]e^{2ift}\Omega^\star=0. \tag{B3}$$

We consider that the background flow and the near-inertial oscillation interact weakly so that the envelope of $\Omega(z,t)$ is evolving slowly relative to the inertial time scale. The secular evolution of $\Omega(z,t)$ (evolution on really long time period) is then obtained by time-averaging (denoted by an overbar) equation (B3) over an interval which is long relative to $f^{-1}$

$$\bar{\Omega}_t+\frac{1}{2}i\zeta\bar{\Omega}+\frac{1}{2}\Upsilon\bar{\Omega}^{\star}=0, \tag{B4}$$

where

$$\zeta\equiv\bar{V}_x-\bar{U}_y, \tag{B5}$$

is the vertical velocity of the low-frequency part of the background flow, assuming that the low-frequency part of the background flow is geostrophycally balanced so that $\bar{W}=\bar{U}_x+\bar{V}_y=0$. The term involving $\frac{1}{2}i\zeta$ in equation (B4) corresponds to Kunze's (1985) result that the effective inertial frequency is shifted away from the local inertial frequency by half the relative vorticity of the low-frequency geostrophic background flow. The second coefficient $\Upsilon$ in equation (B4) is the amplitude of the 2*f*-pump

$$\Upsilon\equiv\overline{\left[\left(U_x-V_y\right)+i\left(V_x+U_y\right)\right]e^{2ift}}, \tag{B6}$$

which is nonzero if the background flow strain rates have spectral content at 2*f*.

Now we consider the propagation of near-inertial oscillations through a geostrophic flow which changes slowly relative to the inertial period. The background flow has two components: a geostrophic component (denoted by subscript *g*) and a 2*f*-pump flow (denoted by subscript *p*). There is no transfer of energy between the geostrophic part of the background flow and the near-inertial waves (Young & Jelloul, 1997). Thus, the 2*f*-pump part of the background flow plays the essential role of energizing the near-inertial oscillations. The dynamics of the near-inertial field $(u,v,w,b,p)$ is given by the linearized Boussinesq equations around the background flow $(U,V,W,B,P)$

$$u_t+Uu_x+Vu_y+Wu_z+uU_x+vU_y+wU_z-fv+p_x=0, \tag{B7}$$

$$v_t+Uv_x+Vv_y+Wv_z+uV_x+vV_y+wV_z+fu+p_y=0, \tag{B8}$$

$$-b+p_z=0, \tag{B9}$$

$$u_x+v_y+w_z=0, \tag{B10}$$

$$b_t+Ub_x+Vb_y+Wb_z+uB_x+vB_y+wB_z+wN^2=0. \tag{B11}$$

We emphasize that PSI is driven solely and essentially by the pump component of the background flow. *Young et al.* [2008]'s calculations lead to the evolution equation of near-inertial fields (*f*-plane, uniform *N*, $\partial_y\equiv0$ and magnitude of $\varpi$ is too small to affect the solution (Young et al., 2008)

$$A_{zzt}+\frac{1}{2}\frac{N^2}{f}iA_{xx}+\frac{1}{2}\Upsilon A^{\star}_{zz}=0, \tag{B12}$$

Considering now the instability of an infinite-plane internal gravity wave with a uniform stratification on an *f*-plane. Its pressure is given by

$$P_p=a\cos\phi, \tag{B13}$$

where $\phi=kx+mz-\omega_0t$ and $a=\frac{U_0h_0m(\omega_0^2-f^2)}{k\omega_0}$ is the amplitude of the pump.

The frequency and the wave number are related by the nonhydrostatic dispersion relation (4). Since, we consider $\omega_0$ close to 2*f*, we write

$$\omega_0=2f+\varepsilon, \tag{B14}$$

with $\varepsilon\ll f$, where the detunning frequency $\varepsilon$, might be either positive or negative; in our case, we consider a negative detuning.

Substituting the pressure into the linearized Boussinesq equations, we obtain the other pump fields

$$U_p=\frac{ak\omega_0}{(\omega_0^2-f^2)}\cos\phi, \tag{B15}$$

$$V_p=\frac{afk}{(\omega_0^2-f^2)}\sin\phi, \tag{B16}$$

$$W_p = -\frac{ak^2\omega_0}{m(\omega_0^2 - f^2)}\cos\phi, \tag{B17}$$

$$B_p = -\frac{ak^2N^2}{m(\omega_0^2 - f^2)}\sin\phi. \tag{B18}$$

From there, we want to calculate the amplitude of the 2*f*-pump from equation (B6), considering $\partial_y \equiv 0$. Thus

$$U_{px} + iV_{px} = \partial_x Re(\tilde{U_p}\, e^{i\phi}) + i\partial_x Re(\tilde{V_p}\, e^{i\phi}) = \frac{iak^2e^{i\phi}}{2(\omega_0 - f)} - \frac{iak^2e^{-i\phi}}{2(\omega_0 + f)} \tag{B19}$$

and therefore

$$\Upsilon = \overline{(U_{px} + iV_{px})e^{2ift}} = i\lambda e^{i(kx+mz-\varepsilon t)}, \tag{B20}$$

where

$$\lambda^2 = \frac{U_0 h_0 k_0^2}{2\omega_0}\sqrt{\frac{(N^2 - \omega_0^2)(\omega_0 + f)}{(\omega_0 - f)}}. \tag{B21}$$

Replacing $\Upsilon 6$ by its expression in equation (B12), we obtain

$$A_{zzt} + \frac{1}{2}\frac{N^2}{f}iA_{xx} + \frac{1}{2}i\lambda e^{i(kx+mz-\varepsilon t)}A^{\star}_{zz} = 0. \tag{B22}$$

The solution of this equation is of the form

$$A = e^{-i\varepsilon t/2}\left[A_1(t)e^{i(k_1x+m_1z)} + A_2^{\star}(t)e^{i(k_2x+m_2z)}\right]. \tag{B23}$$

Now, we use the spatial resonant condition (5) in equation (B23) leading to

$$A_{1t} + i\left(\frac{N^2k_1^2}{2fm_1^2} - \frac{\varepsilon}{2}\right)A_1 + \frac{i\lambda m_2^2}{2m_1^2}A_2 = 0, \tag{B24}$$

$$A_{2t} - i\left(\frac{N^2k_2^2}{2fm_2^2} - \frac{\varepsilon}{2}\right)A_2 - \frac{i\lambda m_1^2}{2m_2^2}A_1 = 0. \tag{B25}$$

Combining the two previous equations, we obtain a single equation for $A_1(t)$

$$A_{1tt} + i\left(\frac{N^2k_1^2}{2fm_1^2} - \frac{N^2k_2^2}{2fm_2^2}\right)A_{1t} + \left(\frac{N^2k_1^2}{2fm_1^2}\frac{N^2k_2^2}{2fm_2^2} - \frac{\lambda^2}{4}\right)A_1 = 0. \tag{B26}$$

If $A_1 = \hat{A}_1 e^{st}$ then

$$s = \frac{1}{2}\left(\frac{N^2k_1^2}{2fm_1^2} - \frac{N^2k_2^2}{2fm_2^2}\right)i \pm \frac{1}{2}\sqrt{\lambda^2 - \left(\frac{N^2k_1^2}{2fm_1^2} + \frac{N^2k_2^2}{2fm_2^2}\right)^2}. \tag{B27}$$

Finally, the growth rate is $\sigma = \mathrm{Re}(s)$, such as

$$\sigma = \frac{1}{2}\sqrt{\lambda^2 - \left(\frac{N^2}{2f}\right)^2\left(\frac{k_1^2}{m_1^2} + \frac{k_2^2}{m_2^2} - 2\frac{\varepsilon f}{N^2}\right)^2}. \tag{B28}$$

**Acknowledgments**
We acknowledge CINES/GENCI, France, for providing access and support to their computing platform OCCIGEN, as well as the PRACE Research Infrastructure computing resource Curie based in France at TGCC. CJM gratefully acknowledges funding from the ANR LEFE program and the ENS Actions Incitatives program. The data used in this study are available upon request from the authors (oceane.richet@csiro.au) or can be downloaded http://doi.org/10.6084/m9.figshare.6061259.

## References

Alford, M. H., MacKinnon, J. A., Zhao, Z., Pinkel, R., Klymak, J., & Peacock, T. (2007). Internal waves across the Pacific. *Geophysical Research Letters*, *34*, L24601. https://doi.org/10.1029/2007GL031566

Bourget, B., Dauxois, T., Joubaud, S., & Odier, P. (2013). Experimental study of parametric subharmonic instability for internal plane waves. *Journal of Fluid Mechanics*, *723*, 1–20.

Bouruet-Aubertot, P., Sommeria, J., & Staquet, C. (1995). Breaking of standing internal gravity waves through two-dimensional instabilities. *Journal of Fluid Mechanics*, *285*, 265–301.

De Lavergne, C., Madec, G., Le Sommer, J., Nurser, A. J. C., & Naveira Garabato, A. C. (2016a). On the consumption of Antarctic Bottom Water in the abyssal ocean. *Journal of Physical Oceanography*, *46*, 635–661.

De Lavergne, C., Madec, G., Le Sommer, J., Nurser, A. J. C., & Naveira Garabato, A. C. (2016b). The impact of a variable mixing efficiency on the abyssal overturning. *Journal of Physical Oceanography*, *46*, 663–681.
Ferrari, R., Mashayek, A., McDougall, T. J., Nikurashin, M., & Campin, J.-M. (2016). Turning ocean mixing upside down. *Journal of Physical Oceanography*, *46*, 2239–2261.
Garrett, C., & Kunze, E. (2007). Internal tide generation in the deep ocean. *Annual Review of Fluid Mechanics*, *39*, 57–87.
Garrett, C., & Munk, W. (1979). Internal waves in the ocean. *Annual Review of Fluid Mechanics*, *11*, 339–369.
Gerkema, T., Staquet, C., & Bouruet-Aubertot, P. (2006). Decay of semi-diurnal internal-tide beams due to subharmonic resonance. *Geophysical Research Letters*, *33*, L08604. https://doi.org/10.1029/2005GL025105
Grisouard, N., & Bühler, O. (2012). Forcing of oceanic mean flows by dissipating internal tides. *Journal of Fluid Mechanics*, *708*, 250–278.
Hazewinkel, J., & Winters, K. (2011). PSI of the internal tide on a $\beta$ plane: Flux divergence and near-inertial wave propagation. *Journal of Physical Oceanography*, *41*, 1673–1682.
Hibiya, T., Nagasawa, M., & Niwa, Y. (2002). Nonlinear energy transfer within the oceanic internal wave spectrum at mid and high latitudes. *Journal of Geophysical Research*, *107*(C11), 3207. https://doi.org/10.1029/2001JC001210
Korobov, A. S., & Lamb, K. G. (2008). Interharmonics in internal gravity waves generated by tide-topography interaction. *Journal of Fluid Mechanics*, *611*, 61–95.
Kunze, E. (1985). Near inertial wave propagation in geostrophic shear. *Journal of Physical Oceanography*, *15*, 544–565.
MacKinnon, J. A., Alford, M. H., Sun, O., Pinkel, R., Zhao, Z., & Klymak, J. (2013). Parametric subharmonic instability of the internal tide at 29°N. *Journal of Physical Oceanography*, *43*, 17–28.
MacKinnon, J. A., & Winters, K. (2005). Subtropical catastrophe: Significant loss of low-mode tidal energy at28.9°. *Geophysical Research Letters*, *32*, L15605. https://doi.org/10.1029/2005GL023376
Marshall, J., Adcroft, A., Perelman, L., & Heisey, C. (1997). A finite-volume, incompressible Navier Stokes model for studies on the ocean on parallel computers. *Journal of Geophysical Research*, *102*, 5753–5756.
Maurer, P., Joubaud, S., & Odier, P. (2016). Generation and stability of inertia-gravity waves. *Journal of Fluid Mechanics*, *808*, 539–561.
McComas, C. H., & Bretherton, F. P. (1977). Resonant interaction of oceanic internal waves. *Journal of Geophysical Research*, *82*, 1397–1412.
Melet, A., Legg, S., & Hallberg, R. (2016). Climatic impact of parameterized local and remote tidal mixing. *Journal of Climate*, *29*, 3473–3500.
Muller, C., & Buhler, O. (2009). Saturation of the Internal Tides and Induced Mixing in the Abyssal Ocean. *Journal of Physical Oceanography*, *39*, 2077–2096.
Munk, W., & Wunsch, C. (1998). Abyssal recipes II: Energetics of tidal and wind mixing. *Deep Sea Research, Part I*, *45*, 1977–2010.
Nikurashin, M., & Ferrari, R. (2013). Overturning circulation driven by breaking internal waves in the deep ocean. *Geophysical Research Letters*, *40*, 3133–3137. https://doi.org/10.1002/grl.50542
Nikurashin, M., & Legg, S. (2011). A mechanisms for local dissipation of internal tides generated at rough topography. *Journal of Physical Oceanography*, *41*, 378–395.
Richet, O., Muller, C., & Chomaz, J.-M. (2017). Impact of a mean current on internal tide energy dissipation at the critical latitude. *Journal of Physical Oceanography*, *47*, 1457–1471.
Staquet, C., & Sommeria, J. (2002). Internal gravity waves: From instabilities to turbulence. *Annual Review of Fluid Mechanics*, *34*, 559–593.
Talley, L. D. (2013). Closure of the global overturning circulation through the Indian, Pacific, Southern Oceans: Schematics and transports. *Oceanography*, *26*, 80–97.
Wunsch, C., & Ferrari, R. (2004). Vertical mixing, energy and the general circulation of the ocean. *Agricultural and Forest Meteorology*, *36*, 281–314.
Young, W. R., & Jelloul, B. M. (1997). Propagation of near-inertial oscillations through a geostophic flow. *Journal of Marine Research*, *55*, 735–766.
Young, W. R., Tsang, Y.-K., & Balmforth, J. (2008). Near-inertial parametric subharmonic instability. *Journal of Fluid Mechanics*, *607*, 25–49.